Research Article

Nano Biomed Eng

Curcumin-loaded PEG-coated Magnetite Nanoparticles Synthesized from *Theobroma cocoa*: Neuronal Biocompatibility and Anti-inflammatory Properties in SH-SY5Y and RAW 264.7 Cells

Mohamed Abdelmonem[1,2], Norazalina Saad[3], Huey Fang Teh[5], Ahmad Kamil Mohd Jaaffar[6,7], Mohamed Ahmed Ibrahim[2,8], Maha A. Alhadad[9], Che Azurahanim Che Abdullah[1,3,4]✉

[1] Department of Physics, Faculty of Science, Universiti Putra Malaysia, 43400 UPM Serdang, Selangor Darul Ehsan, Malaysia
[2] Department of Pharmaceutics and Industrial Pharmacy, Faculty of Pharmacy, October University for Modern Sciences and Arts (MSA), Giza 12451, Egypt
[3] Laboratory of Cancer Research UPM-MAKNA (CANRES), Institute of Bioscience, Universiti Putra Malaysia, 43400 UPM Serdang, Selangor Darul Ehsan, Malaysia
[4] Nanomaterial Synthesis and Characterization Lab, Institute of Nanoscience and Nanotechnology, Universiti Putra Malaysia, 43400 UPM Serdang, Selangor Darul Ehsan, Malaysia
[5] SD Guthrie Technology Centre Sdn Bhd, Lebuh Silikon, Universiti Putra Malaysia, 43400 UPM Serdang, Selangor Darul Ehsan, Malaysia
[6] Lembaga Koko Malaysia, Tingkat 5-7, Wisma SEDCO, Lorong Plaza Wawasan, Off Coastal Highway, Beg Berkunci 211, Kota Kinabalu 88999, Sabah, Malyasia
[7] Pusat Inovasi & Teknologi Koko Nilai, Lot 12621, Kawasan Perindustrian Nilai, Nilai 71800, Negeri Sembilan Darul Khusus, Malaysia
[8] Natural Medicines and Products Research Laboratory, Institute of Bioscience, Universiti Putra Malaysia, 43400 UPM Serdang, Selangor Darul Ehsan, Malaysia
[9] Department of Pharmacology & Toxicology, Faculty of Pharmacy, October University for Moder Sciences and Arts (MSA), Giza 12451, Egypt

✉ Corresponding author. E-mail: azurahanim@upm.edu.my

Received: Aug. 18, 2024; **Revised:** Sep. 5, 2024; **Accepted:** Oct. 7, 2024

Citation: M. Abdelmonem, N. Saad, H.F. Teh, et al. Curcumin-loaded PEG-coated magnetite nanoparticles synthesized from *Theobroma cocoa*: neuronal biocompatibility and anti-inflammatory properties in SH-SY5Y and RAW 264.7 cells. *Nano Biomedicine and Engineering*, 2024, 16(3): 386−401.

http://doi.org/10.26599/NBE.2024.9290099

Abstract

Neurodegenerative diseases (NDDs) encompass numerous disorders affecting the nervous system's structure and functions, primarily caused by protein aggregation, oxidative stress, and inflammation. These factors make a significant contribution to the progression of various NDDs. Curcumin (CUR), a natural bioactive compound known for its anti-inflammatory and antioxidant properties, has limited application because of its hydrophobicity. To address this issue, PEGylated coated magnetite nanoparticles (MNPs) were developed as efficient nanocarriers. These MNPs were synthesized using plant polyphenols from cocoa bean (*Theobroma cacao*) shell extract, coated with PEG, and then loaded with CUR at various concentrations. The nanomaterials were characterized using X-ray diffraction (XRD), Dynamic light scattering (DLS), zeta potential (ZP), FTIR, Transmission electron microscopy (TEM), selected-area electron diffraction (SAED), and vibrating sample magnetometer (VSM). The nanoparticles were found to be spherical, with diameters in the range of 10–19 nm. VSM analysis showed that the MNPs exhibited superparamagnetic behavior at room temperature. *In vitro*

studies using ultraviolet (UV) spectrophotometry revealed rapid CUR drug loading within 3 h and total drug release of 57% over 48 h, indicating the potential of the MNPs as a neuroprotective agent. The cell viability associated with exposure to the nanoformulations was also assessed in human neuroblastoma cells (SH-SY5Y) using the MTT assay. In addition, the safety and anti-inflammatory properties of PEGylated MNPs–CUR were evaluated in LPS-induced murine macrophages (RAW 264.7). Cells exposed to the nanoparticles exhibited high viability, indicating their safety for human neuroblastoma cells, and the nanoparticles effectively reduced nitric oxide production in murine macrophages. These findings suggest that PEGylated MNPs–CUR possess significant potential as neuroprotective agents for brain-related diseases, given their biosafety and anti-inflammatory properties.

Keywords: neurodegenerative disease; magnetic nanoparticle; green synthesis; RAW 264.7 cell; SH-SY5Y cell

Introduction

Neurodegenerative diseases (NDDs), such as Alzheimer's, Parkinson's, and Huntington's diseases and multiple sclerosis, involve the gradual loss of neural cell function in the brain or peripheral nervous system [1]. Despite differences in their mechanisms and progression, these diseases share common features, including neuroinflammation, neuron loss, protein misfolding, oxidative stress, and disrupted autophagy [2, 3]. Neuroinflammation, triggered by damaged neurons, microbes, harmful chemicals, or abnormal proteins like amyloid beta, plays a significant role in NDDs [4].

Current therapies for NDDs exhibit limited efficacy and are associated with severe adverse effects, including anemia, reproductive complications, neurotoxicity, and gastrointestinal disturbances, which significantly diminish patients' quality of life [5]. Furthermore, the systemic delivery of drugs to the central nervous system (CNS) presents a considerable challenge due to limited brain accessibility, extensive first-pass metabolism, reduced drug half-life, and potential off-target effects in peripheral tissues. Although various endogenous proteins and antibody-based biopharmaceuticals have been proposed and evaluated for treating NDDs, their therapeutic efficacy remains inadequate [6]. There is thus growing interest in natural polyphenols, particularly curcumin (CUR), given its strong antioxidant and anti-inflammatory properties [7]. CUR has shown promise in treating various NDDs, and its fluorescent capabilities make it a potential tool for diagnosing different NDDs [8, 9].

Nanotechnology focuses on developing materials and structures between 1 and 100 nm in size, at which scale unique physicochemical and biological properties emerge due to large surface area relative to size [10, 11]. Magnetic nanoparticles, particularly iron oxide nanoparticles (IONPs), are valuable in bioanalytical and biomedical applications because they minimize background interference in biological specimens [12]. Among the different phases of IONPs, magnetite nanoparticles (MNPs) are most commonly used due to their unique electrical and magnetic properties, especially in biomedical applications where their sub-20 nm size allows them to exhibit superparamagnetism [13–15]. To enhance the performance of these nanoparticles, polyethylene glycol (PEG) has been used as a synthetic biodegradable and biocompatible polymer to coat MNPs. PEGylation on the surface reduces plasma protein binding, slows the clearance of nanoparticles by the mononuclear phagocyte system, and extends their circulation time, thereby improving the efficacy of PEGylated nanoformulations in biomedical applications [16, 17].

The green chemistry synthesis of MNPs provides biocompatible, stable, and nontoxic nanomaterials, making it a valuable approach for biomedical applications [18]. The beans of the cacao tree, *Theobroma cacao*, contains bioactive compounds like polyphenols and tocopherols, which can act as reducing and stabilizing agents for MNP synthesis. Furthermore, cocoa beans' bioactive compounds were found to exert neuroprotective effects that may help manage NDDs [19, 20].

In the literature, there are no reports of studies

assessing the cytotoxicity of biogenic MNPs specifically synthesized in a *Theobroma cocoa*-mediated manner loaded with CUR in human neuroblastoma cells (SH-SY5Y) or their effect on nitric oxide (NO) inhibition in macrophage RAW 264.7 cells. This study was implemented to synthesize MNPs using cocoa bean shell (CBS) extract, subsequently functionalize them with PEG (M_w = 2 000 Da), and incorporate CUR to develop an agent with potential neuroprotective effects. We assessed the *in vitro* cytotoxicity of these nanomaterials in SH-SY5Y cells, and also evaluated their anti-inflammatory effect by measuring the reduction of NO production induced by lipopolysaccharide (LPS) in RAW 264.7 cells, mimicking the neuroinflammation associated with NDDs.

Materials and Methods

Reagents and materials

Cocoa bean shells were sourced from the Malaysian Cocoa Board in Kota Kinabalu, Sabah, Malaysia. Iron(II) chloride tetrahydrate ($FeCl_2 \cdot 4H_2O$, 99%) and iron(III) chloride ($FeCl_3 \cdot 6H_2O$, 99%), used in the synthesis of biogenic superparamagnetic magnetite, as well as polyethylene glycol (M_w = 2 000 Da) for coating the magnetite nanoparticles, were procured from Sigma Aldrich. CUR with a purity of 95% was also acquired from Sigma Aldrich. The SH-SY5Y human neuroblastoma cell line (ATCC® CRL-2266™) was kindly supplied by the Institute of Bioscience at Universiti Putra Malaysia. The RAW 264.7 mouse macrophage cell line (ATCC TIB-71) was obtained from Nawah Scientific Inc. (Cairo, Egypt). 3-(4,5-Dimethylthiazol-2-yl)-2,5-diphenyltetrazolium bromide (MTT) was purchased from Thermo Fisher Scientific. Dulbecco's Modified Eagle Medium (DMEM), Roswell Park Memorial Institute (RPMI) 1640 medium, fetal bovine serum (FBS), and penicillin–streptomycin (Penstrip) antibiotics were sourced from Capricorn Scientific (Germany).

Preparation of CBS extract, MNPs, and PEGylated MNPs

Briefly, the CBS extract was washed with ultrapure water and air-dried. The dried shells were ground into a fine powder. To prepare the CBS extract, 10 g of the powder was added to 100 ml of deionized water, heated, and stirred for 40 min. After filtering, the aqueous extract was stored at 4 °C for future use. To prepare the MNPs, the CBS extract was slowly added to a mixture of ferric and ferrous salts while continuously stirring. NaOH was then added until the mixture became alkaline. The mixture was then stirred until a color change indicated MNP formation. The pellets were then separated by centrifugation, washed with acetone, and dried in a hot air oven. After drying, they were stored in an airtight container for future use. To prepare the PEGylated MNPs, the MNPs were dispersed in distilled water and then added to a PEG solution. The mixture was mechanically stirred, and the resulting sample was centrifuged to obtain PEGylated MNP pellets. These pellets were washed three times with ethanol, dried in the oven, and stored in an airtight container for further analysis.

Preparation of PEGylated MNPs–CUR

Ten milligrams of CUR was dissolved in 10 mL of ethanol to achieve a concentration of 1 mg/mL. Subsequently, this CUR solution in ethanol was gradually added to an aqueous dispersion of MNPs, which consisted of 200 mg of particles in 10 mL of water. The resulting mixture was stirred at 400 r/min at room temperature for 3 h to allow the CUR molecules to permeate the PEG polymer layers surrounding the nanoparticle core [21]. After this period, the mixture was centrifuged three times at 6 000 r/min for 10 min each to separate the pellets from the supernatant. The pellets were then collected, dried, and stored in a tightly sealed container. This procedure was also repeated with different CUR concentrations of 1, 2, and 3 mg/mL.

Characterization of MNPs, PEGylated MNPs, and PEGylated MNPs–CUR

The MNPs, PEGylated MNPs, and PEGylated MNPs–CUR were analyzed using various instruments. X-ray diffraction (XRD) was performed with the MXP3V (Mac Science, Japan). Dynamic light scattering (DLS) and zeta potential (ZP) measurements were carried out using the Zetasizer Nano ZS90 (Malvern, UK). Fourier transform infrared (FTIR) spectroscopy was conducted with the Spectrum 100 (Perkin Elmer, USA). Field emission scanning electron microscopy combined with energy-dispersive X-ray spectroscopy was performed using

the JSM 7600F (JOEL, USA). Transmission electron microscopy (TEM) was performed with the Tecnai TF20 X-Twin (FEI Company, USA), magnetic properties were measured with a vibrating sample magnetometer (VSM, Model 7404; Lake Shore, USA), and ultraviolet–visible (UV–Vis) spectroscopy was conducted using the SP-LUV752P spectrophotometer (Bioevopeak, China) to measure absorbance for drug loading and *in vitro* release studies.

CUR loading content and entrapment efficiency

To determine the loading efficiency of CUR, 1.0 mg of the dry nanoparticles containing CUR were dissolved in ethanol and then subjected to water bath sonication at room temperature in the dark to fully extract the CUR into the solution. The ethanol solution of PEGylated MNPs containing CUR was then centrifuged at 6 000 r/min to separate the MNPs from the CUR. Clear yellow supernatants were collected for analysis. The CUR concentration in each supernatant was measured using the UV–Vis spectrophotometer at 428 nm. A standard curve of CUR in ethanol ranging from 0 to 20 μg/mL was prepared under identical conditions. The CUR loading content (LC%) and entrapment efficiency (EE%) values were calculated using the following formulas:

$$\mathrm{LC\%} = \frac{W_{\text{drug in nanoparticles}}}{W_{\text{nanoparticles}}} \times 100 \quad (1)$$

$$\mathrm{EE\%} = \frac{W_{\text{drug in nanoparticles}}}{W_{\text{initial amount of drug added}}} \times 100 \quad (2)$$

In vitro release studies

The release profile of the drug was studied in a PBS (pH 7.4) medium under reservoir (r)–sink (s) conditions at 37 °C. In brief, 5 mg of PEGylated MNPs–CUR were placed in a dialysis bag containing 3 mL of PBS:ethanol with a pH of 7.4. This dialysis bag (reservoir) was then immersed in 40 mL of the same buffer medium. To improve the dissolution of CUR in consideration of its hydrophobicity, 50% ethanol solution was added to the release medium at a ratio of 1:1 with PBS [22, 23]. Subsequently, 2 mL of the release medium was removed at specific time intervals (0.5, 1, 2, 4, 8, 12, 24, and 48 h) and replaced with fresh medium. The absorbance of these samples was measured using a UV spectrophotometer at 428 nm. The *in vitro* release of CUR from the nanoparticles was determined using a standard curve of CUR prepared in ethanol/PBS (1:1, v/v) solutions at various concentrations. All experiments were conducted in triplicate for each timepoint.

Cell culture

SH-SY5Y cells were cultured in a 1:1 mix of DMEM and Ham's F-12 medium, supplemented with 10% heat-inactivated FBS and 1% Penstrep. RAW 264.7 cells, kindly provided by Nawah Scientific Inc. (Egypt), were cultured in DMEM with 10% FBS, 2 mM L-glutamine, and 1% Penstrep. Both cell lines were grown under standard conditions (37 °C and 5% CO_2) until they reached 70%–80% confluence, prior to any further experimentation.

Cell viability using MTT and SRB assays in the SH-SY5Y and RAW 264.7 cell lines

Cell viability was assessed using two different assays: the MTT assay for SH-SY5Y cells and the SRB assay for RAW 264.7 cells. For the MTT assay, SH-SY5Y cells were seeded in 96-well plates at a density of 1×10^4 cells/mL and incubated overnight. The cells were then treated with various concentrations of MNPs, PEGylated MNPs, and PEGylated MNPs–CUR (1.56–100 μg/mL) and incubated for 48 h. Following this, the growth medium was removed, and 20 μL of 5 mg/mL MTT solution was added to each well. Plates were incubated in the dark for 3 h, after which 100 μL of DMSO was added to dissolve the formazan crystals. Absorbance was measured at 570 nm using an ELISA plate reader to calculate cell viability relative to that in the control groups.

For the SRB assay, RAW 264.7 cells were seeded in 96-well plates with 100 μL of cell suspension (5×10^3 cells) and incubated in complete medium for 24 h. The cells were then treated with drugs at the same drug concentrations used for the previously mentioned cells (1.56–100 μg/mL) in an additional 100 μL of medium. After drug treatment, the cells were fixed with 150 μL of 10% TCA at 4 °C for 1 h, washed with distilled water, stained with 0.4% SRB solution for 10 min, washed with 1% acetic acid, and allowed to air-dry overnight. The protein-bound SRB stain was dissolved with 150 μL of 10 mmol/L Tris, and the absorbance was measured at 540 nm using an Infinite F50 microplate reader. Cell viability was calculated relative to the control groups using the

absorbance values based on the following formula:

$$\text{Cell viability} = \left(\frac{\text{Absorbance sample (mean)}}{\text{Absorbance control (mean)}}\right) \times 100 \quad (3)$$

The cell viability rate at different concentrations was plotted in accordance with a previously reported method [24], and all experiments were repeated in triplicate.

Nitric oxide inhibition assay

RAW264.7 cells were seeded in a 96-well plate and incubated for 24 h. The following day, inflammation was induced using 1 μg/mL LPS (LPS group), while the control group cells were replenished with fresh medium. Compounds were administered with LPS at two to five different concentrations (LPS + drug group). Quercetin at 300 μg/mL was used as a positive control for its anti-inflammatory effects. To assess NO secretion, equal volumes of the cell supernatant and Griess reagent were mixed and incubated for 10 min in the dark at room temperature. The absorbance at 540 nm, indicating the nitrite concentration, was measured using an ELISA plate reader.

Statistical analysis

Data were analyzed using GraphPad Prism software version 9. Analysis of variance was conducted to assess the impact of each treatment compared with the control and to identify differences among the groups. Results are reported as mean ± standard deviation (SD) for three sample measurements. A *P*-value of ≤ 0.05 was considered statistically significant.

Results and Discussion

Dynamic light scattering (DLS)

The hydrodynamic size of the MNPs was determined to be 115.6 ± 0.6 nm, with a polydispersity index (PDI) of 0.178 ± 0.02. In contrast, the hydrodynamic size of the PEGylated MNPs was measured to be 69.19 ± 0.5 nm, with a PDI of 0.197 ± 0.01. As shown in Fig. 1, there was a significant reduction in size from 115.6 nm to 69.19 nm following the PEGylation process, suggesting that PEG effectively minimizes aggregation. This size reduction was attributed to the propensity of PEG molecules to form a coiled structure at low surface densities, effectively

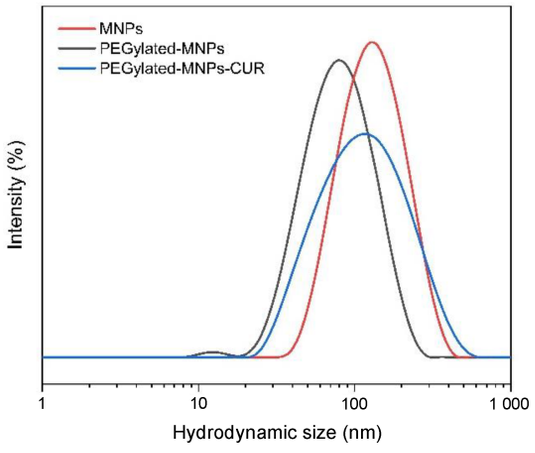

Fig. 1 Hydrodynamic size of magnetite nanoparticles (MNPs), PEGylated-MNPs, and PEGylated-MNPs-CUR.

encapsulating the nanoparticles [17, 25]. These results are consistent with numerous previous studies that demonstrated the impact of PEGylation on reducing the hydrodynamic size of synthesized nanoparticles. For example, Tai et al. (2016) reported a decrease in the hydrodynamic size following the addition of PEG 600 Da to MNPs [26]. Similarly, Panday et al. (2020) observed a reduction in size from 93.13 to 79.20 nm when PEG was incorporated into PEI-MNPs [27]. Upon the addition of CUR to the PEGylated MNPs, the hydrodynamic size increased to 98.63 ± 1.7 nm. This increase in size from 69 nm to 98 nm suggests that CUR was loaded within the PEG polymer. Moreover, the PDI value of PEGylated MNPs–CUR was 0.276 ± 0.011, indicating excellent polydispersity. Across all three formulations, the sizes were sufficiently small, making them suitable for biomedical applications, particularly as neuroprotective agents.

Zeta potential (ZP)

Evaluation of the stability of MNPs is essential before their application in the biomedical field. To perform this, ZP analysis was carried out to measure the surface charge of the MNPs, PEGylated MNPs, and PEGylated MNPs–CUR. As depicted in Fig. 2, the ZP values were −40.6 ± 0.65 mV for MNPs (Fig. 2(a)), −35.7 ± 0.15 mV for PEGylated MNPs (Fig. 2(b)), and −38.4 ± 1.93 mV for PEGylated MNPs–CUR (Fig. 2(c)), indicating excellent stability for all formulations. The negative values are mainly due to of attached hydroxyl $(OH)^-$ ions on the MNPs' surface in a basic medium (pH 10). In the literature, it is suggested that a ZP value above ± 30 mV indicates high stability in the formed NP dispersions [28, 29].

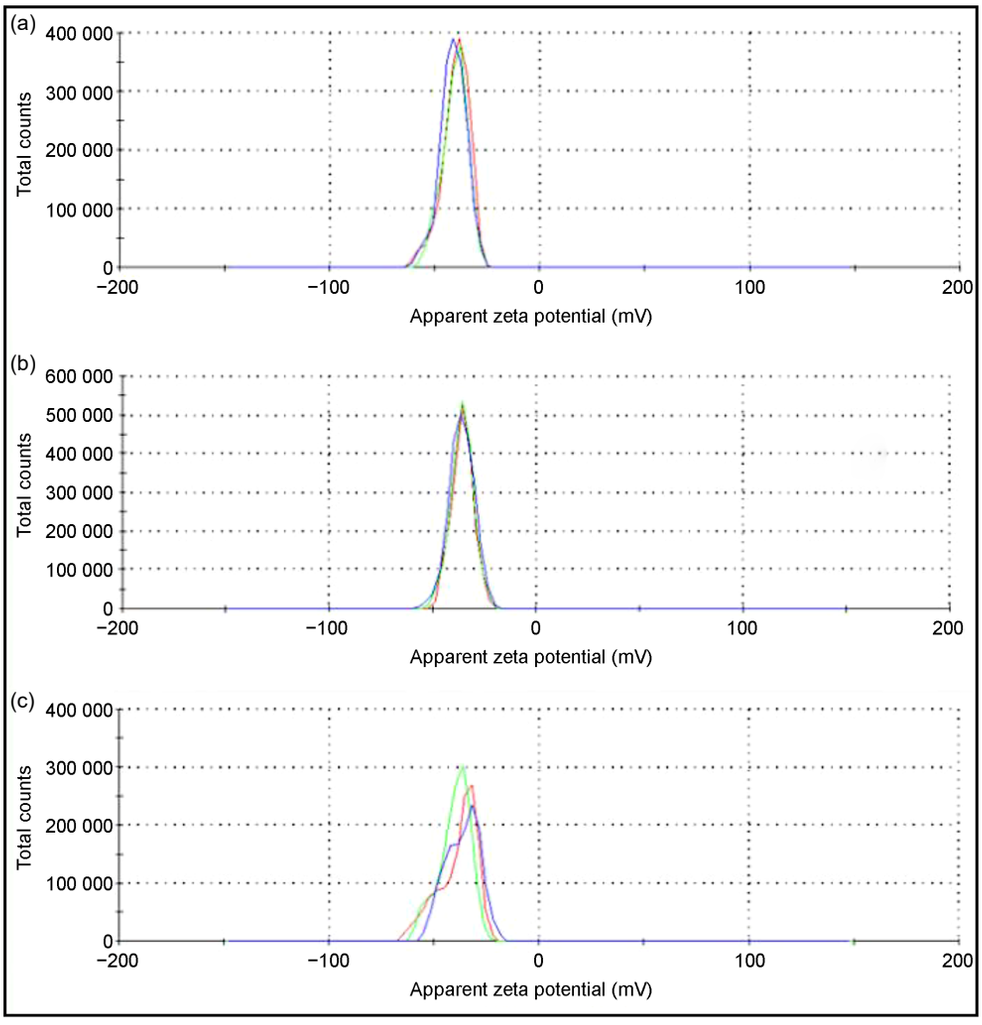

Fig. 2 Zeta potential (ZP) of **(a)** magnetite nanoparticles (MNPs), **(b)** PEGylated MNPs, and **(c)** PEGylated MNPs–CUR.

Conversely, lower ZP values can lead to particle aggregation and flocculation due to van der Waals forces among the iron NPs, causing physical instability. These ions can affect the surface charge and potentially reduce the stability under certain conditions [30].

Fourier transform infrared (FTIR) spectroscopy

Figure 3 depicts the FTIR spectra of MNPs, PEGylated MNPs, and PEGylated MNPs–CUR. In the FTIR spectrum of the MNPs, the presence of two distinctive peaks at 560 and 578 cm^{-1}, which are associated with the Fe–O bond, confirms the exclusive formation of the magnetite phase. This observation effectively rules out the presence of other iron oxide phases, such as goethite or hematite, in the synthetic process [31]. These findings are corroborated by comparing the FTIR spectrum with those reported in previous studies [32, 33]. Indeed, the FTIR spectrum of magnetite displays prominent bands in the low-frequency range (1 000–500 cm^{-1}), which are characteristic of the iron oxide structure [34]. Furthermore, the observed peak at 1 604 cm^{-1} corresponds to the C=C stretching vibration groups, while the peak at 1 384 cm^{-1} confirms the O–H bending vibration of the alcohol/phenol groups that may be present in the CBS extract [35]. In the FTIR spectrum of the PEGylated MNPs, distinct spectral features are observed. The main absorbance peak for the ether stretch band occurs at 1 074 cm^{-1}, while bending vibrations of the $–CH_2$ and –CH groups are noted at 1 477 cm^{-1} and 1 270 cm^{-1}, respectively. The bending of H–O–H is evident around 1 600 cm^{-1}. The Fe–O vibration characteristic of the PEGylated MNPs is observed around 559 and 542 cm^{-1}. A broad peak at 3 365 cm^{-1} in PEGylated MNPs indicates the presence OH groups. These observations, including the C–O–C ether stretch, –CH, $–CH_2$ bending, H–O–H bending, and Fe–O stretching, collectively confirm the successful coating of the MNP surface with PEG. As for the IR spectrum of the PEGylated MNPs–CUR,

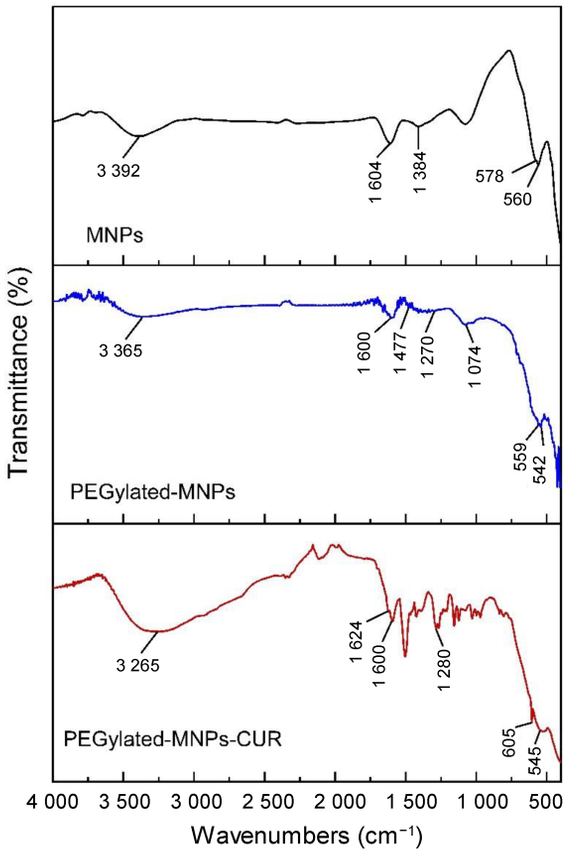

Fig. 3 FTIR spectra of magnetite nanoparticles (MNPs), PEGylated MNPs, and PEGylated MNPs–CUR.

the peak at 1 624 cm^{-1} corresponds to vibration of the C=O bond, which overlaps with the C=C bond. The band at 1 600 cm^{-1} is attributed to stretching vibration of the C=C aromatic ring. Furthermore, the aromatic C–O stretching peak of CUR can be seen at 1 280 cm^{-1} in the conjugated system. All of the aforementioned peaks indicate the successful loading of CUR in the conjugate system [21]. The FTIR spectrum of the PEGylated MNPs–CUR shows combined characteristic peaks of CUR and MNPs.

X-ray diffraction (XRD)

The XRD patterns of MNPs, PEGylated MNPs, and PEGylated MNPs–CUR are presented in Fig. 4. The diffraction peaks observed at 2θ values of 30.21°, 35.5°, 43.31°, 53.80°, 57.3°, and 62.7° correspond to the (220), (311), (400), (422), (511), and (440) Bragg reflections, respectively, which align closely with the spinel structure of pure magnetite, as indicated by JCPDS card No. 19-0629 (Fig. 4(a)) [36]. The XRD pattern for the PEGylated MNPs demonstrates that the PEG coating does not affect the crystalline structure of the magnetite, as depicted in Fig. 4(b). The observed lower peak intensity for the PEGylated

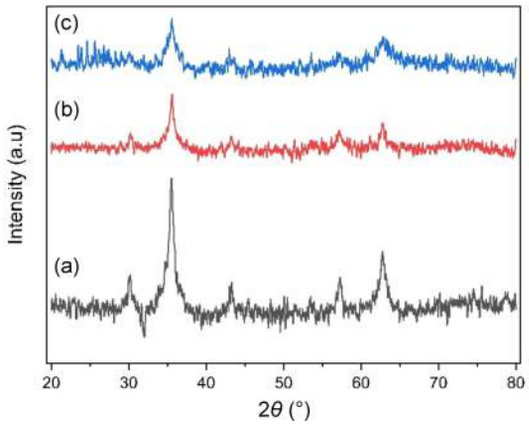

Fig. 4 XRD patterns of **(a)** magnetite nanoparticles (MNPs), **(b)** PEGylated MNPs, and **(c)** PEGylated MNPs–CUR.

MNPs compared with that for the bare MNPs suggests the presence of a PEG coating on their surface [37]. Regarding the pattern of PEGylated MNPs–CUR (Fig. 4(c)), the peaks in the composite particles indicate that the encapsulation of CUR does not alter the phase of the core MNPs. However, the intensity of these characteristic peaks is significantly reduced, possibly due to the linkage of CUR with the core MNPs within the polymer matrix. Additionally, multiple small peaks between 20° and 30° correspond to the presence of CUR [38], further indicating its successful encapsulation in the PEGylated MNPs.

High-resolution transmission electron microscopy (HR-TEM) and selected-area electron diffraction (SAED)

Figure 5 shows the TEM images and SAED patterns for MNPs, PEGylated MNPs, and PEGylated MNPs–CUR. The bare MNPs (Fig. 5(a)) showed some aggregation, while the PEGylated MNPs (Fig. 5(b)) exhibited significantly less aggregation, indicating that the PEG coating reduced aggregation and improved dispersibility. For the PEGylated MNPs–CUR, as can be seen in Fig. 5(c), the changes in illumination suggest a core-shell structure, with the lighter areas representing the CUR-loaded molecules and the darker ones indicating the MNP core. The SAED patterns for all nanomaterials show diffraction intensities that match the crystalline structure of magnetite, similar to the XRD patterns for the three compounds. This suggests that the PEGylation process after synthesis does not change the core size, but may affect the hydrodynamic size. Moreover, the shape and size of the SAED rings in the PEGylated MNPs–CUR showed that the magnetite core remained unchanged after encapsulation, suggesting

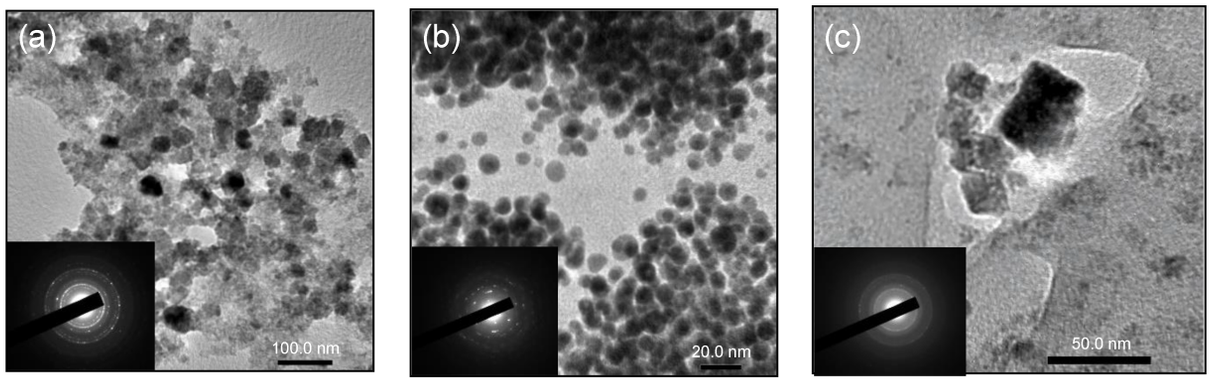

Fig. 5 TEM images and SAED patterns of **(a)** magnetite nanoparticles (MNPs), **(b)** PEGylated MNPs, and **(c)** PEGylated MNPs–CUR.

that the nanoparticles retained their magnetic properties [39]. The core sizes of the samples were almost the same, within the measurement error, with mean particle diameters of 10 ± 2.7 nm for bare MNPs, 11.8 ± 0.94 nm for PEGylated MNPs, and 19.3 ± 1.586 nm for PEGylated MNPs–CUR. The increase in size of the CUR-conjugated system likely indicates successful CUR encapsulation within the PEG-coated nanoparticles. The final size of approximately 19 nm is beneficial for crossing the blood–brain barrier (BBB). Research has shown that, as the nanoparticle size decreases, the permeability through BBB gaps increases, with particles larger than 200 nm showing minimal permeation [40]. Additionally, because PEGylated MNPs–CUR are larger than 5 nm, they will not be subject to renal filtration [41]. A study by Ohta et al. revealed that 15 nm gold nanoparticles were more efficiently delivered into the mouse brain than 3 nm and 120 nm particles [42]. This supports the potential of PEGylated MNPs–CUR as an effective neuroprotective agent.

Vibrating sample magnetometer (VSM)

Figure 6 presents the magnetic field versus magnetic moment (*M*-*H*) curves for MNPs, PEGylated MNPs, and PEGylated MNPs–CUR. The VSM curves for the three samples exhibit a sigmoidal shape devoid of a hysteresis loop, indicative of their superparamagnetic properties. Superparamagnetism implies that these nanoparticles aggregate under a magnetic field due to the magnetic dipole attraction. Notably, this aggregation is reversible, dissipating upon removal of the magnetic field, resulting in no residual magnetization. This superparamagnetic behavior is particularly beneficial for biomedical applications. The saturation magnetization (M_s) values were

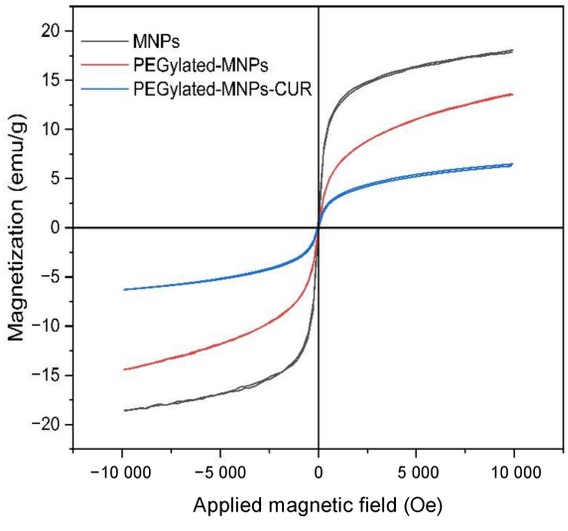

Fig. 6 VSM curves for MNPs, PEGylated MNPs, and PEGylated MNPs–CUR

recorded at 18 emu/g for MNPs, 14 emu/g for PEGylated MNPs, and 6.4 emu/g for PEGylated MNPs–CUR. These values correlate with the nanoparticles' small sizes, as M_s typically decreases with smaller particles [43]. These *M* values are within the acceptable range, confirming their suitability for biomedical applications. Furthermore, both materials exhibited low coercivity, measured at 19.29, 23.71, and 37.229 Oe, and very low remanence (M_r), with values of 0.63, 0.33, and 0.25 emu/g for MNPs, PEGylated MNPs, and PEGylated MNPs–CUR, respectively. The notably low coercive forces and remanence minimize the magnetic dipolar interactions among the nanoparticles, significantly reducing the risk of complications, such as blood clots [44]. Regarding PEGylated MNPs–CUR, the reduction in the magnetic response is primarily due to disruption of the surface spin alignment caused by the polymer and drug molecules. This surface spin disorder decreases the overall magnetization of the

nanoparticles, while the particles retain their superparamagnetic behavior. All of the presented magnetic values are still sufficient for effectively guiding the particles to the target site for drug delivery using an external magnetic field [45, 46].

CUR encapsulation efficiency and drug loading

To quantify the CUR loaded into the PEGylated MNPs–CUR, a standard curve was established using known concentrations of CUR dissolved in ethanol and analysis with a UV–Vis spectrophotometer at a wavelength of 428 nm. Using this method, the loading percentages across three different concentrations (1, 2, and 3 mg/mL, marked as CUR 1, CUR 2, and CUR 3, respectively) were determined. Table 1 outlines the LC% and EE% values for each concentration. The maximum LC% and EE% observed were 36.56% ± 4.60% and 75.57% ± 9.5%, respectively, with a CUR concentration of 2 mg/mL. This efficiency decreased to 48.7% ± 2.04% when the amount of feed drug was increased. A comparable LC% value of 38.0% was reported in a study conducted by Shen et al., where they utilized a poly(vinyl anisole)@PEG (PVAS@PEG) platform for CUR encapsulation [47]. In contrast, our study demonstrated higher loading capacity values than in other studies that used PEG polymers for CUR encapsulation [48, 49]. Notably, increased LC% values can be achieved by using polymers with higher molecular weights [50]. Owing to the favorable LC% and EE%, the 2 mg/mL CUR sample was selected for further *in vitro* drug release studies.

Table 1 Encapsulation efficiency and loading capacity of CUR in different PEGylated MNPs–CUR.

Samples	Average LC%	Average EE%
CUR 1	11.83% ± 1.14%	24.82% ± 2.39%
CUR 2	36.56% ± 4.60%	75.57% ± 9.50%
CUR 3	39.14% ± 2.54%	48.70% ± 2.04%

In vitro drug release

Approximately 56% of the encapsulated CUR was released within 72 h, as shown in Fig. 7. This release rate is notable higher when compared with other reported maximum drug release values [51, 52]. The release profile exhibited a burst of release within the first 24 h, which then gradually decreased, eventually reaching a plateau after 72 h. This release pattern can

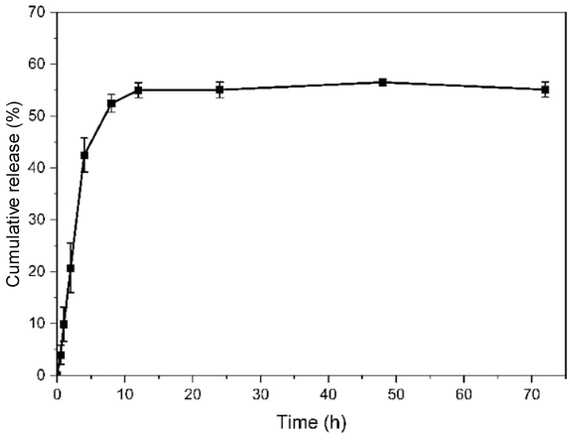

Fig. 7 *In vitro* release profile of CUR from PEGylated MNPs–CUR in PBS (pH 7.4).

be attributed to the small size of the MNPs, which results in a higher surface-to-volume ratio, thereby enhancing the intensity of the initial burst release [53]. Additionally, the use of low-molecular-weight PEG (2000 Da) likely contributed to the quick-release kinetics [50, 54, 55]. The remaining 44% of CUR that was not released after 72 h may have been due to the intermolecular hydrogen bonding between CUR and the PEG polymer, which inhibits further release from the nanoparticle matrix [56]. The results obtained in this study align with the findings of Rachmawati et al., who reported a maximum release rate of 54.43% over 48 h for curcumin-loaded PLA nanoparticles in PBS at pH 7.4 and 37 °C. Similarly, the formulation in this study exhibited a comparable release profile, with an initial burst release of 44% observed within the first 12 h [57]. Moreover, in a study conducted by Bisht et al., the release kinetics of curcumin indicated approximately 40% release from the polymer after 24 h when dispersed in a phosphate buffer at physiological pH [58].

The *in vitro* drug release was evaluated using several kinetic models, including the zero-order, first-order, Korsmeyer–Peppas, and Higuchi models, as shown in Fig. 8. The zero-order release mechanism characterizes a scenario where the drug release rate remains constant and is independent of the drug concentration. In contrast, the first-order release mechanism is concentration-dependent, with the release rate diminishing as the drug concentration decreases [59]. The Higuchi model describes the drug release from an insoluble matrix as proportional to the square root of time, indicative of Fickian diffusion [60, 61]. Finally, the Korsmeyer–Peppas model uses mathematical equations to describe drug release from

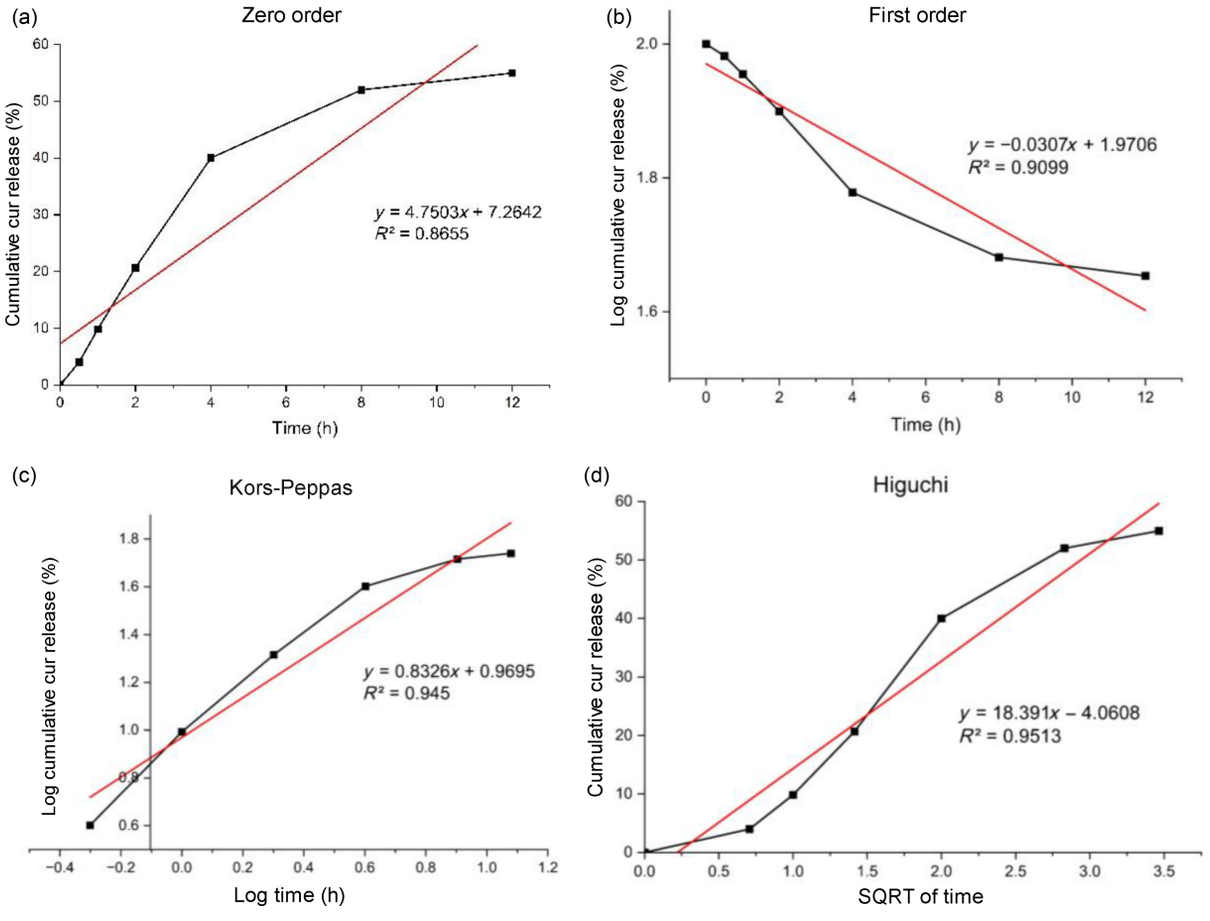

Fig. 8 Kinetic analysis plots for curcumin (CUR) release: **(a)** zero-order, **(b)** first-order, **(c)** Korsmeyer– Peppas, and **(d)** Higuchi models.

a polymeric system [62]. The equations for these models are provided below (Eqs. (4)–(7)).

$$C = K_0 t \tag{4}$$

where C denotes the drug concentration at time t, where t is the time and k_0 is the zero-order rate constant, expressed in units of concentration per time.

$$\log C_0 - \log C = \frac{k_1 t}{2.303} \tag{5}$$

In this equation, C_0 represents the initial drug concentration and k_1 is the first-order rate constant.

$$C = K_H \sqrt{t} \tag{6}$$

Here, K_H is a constant reflecting the design variables of the system.

$$\frac{M_t}{M_\infty} = K_H t^n \tag{7}$$

Here, $M_\infty M_t$ represents the proportion of the drug released at time t, where t is the release time. K_H is the kinetic rate constant of the Korsmeyer–Peppas model, and n is the release exponent indicating the drug release mechanism.

Upon analyzing the release kinetics, it was determined that the Higuchi model most accurately described the release data, with the highest R^2 value of 0.951. This suggests that the release of CUR from PEGylated MNPs was primarily diffusion-controlled, indicating an anomalous (non-Fickian) release mechanism. According to the Higuchi model, drug release from PEGylated MNPs involves the drug penetrating and dissolving within the polymeric matrix, followed by diffusion through the polymeric pores into the external environment. This behavior is typically observed in hydrophilic matrix systems, aligning with the properties of the composite formulated in this study. Consequently, the rate of CUR release from the polymeric system demonstrates that both swelling and erosion of the polymer occur simultaneously. These findings are consistent with those of several previous studies. For instance, a study by Reddy et al. developed sodium alginate/ montmorillonite microbeads encapsulating CUR, which best fit the Higuchi model with an R^2 value of 0.983, indicating diffusion-controlled release [63].

RAW 264.7 cell line

Cell viability assay

Assessing the cytotoxic effects of the formulation on normal macrophages was a pivotal aspect. Different types of nanoparticles have been reported to enter macrophages through both phagocytic and nonphagocytic pathways [64], potentially disrupting mitochondrial function [65]. Consequently, ensuring safety is essential in the development of new medications. The effect of PEGylated MNPs–CUR on the viability of RAW 264.7 cells was assessed using an SRB assay with the concentration range of 0.1–100 μg/mL, with the results presented in Fig. 9. This concentration range was carefully selected on the basis of previous research involving RAW 264.7 cells, ensuring that the results are comparable with established studies [66–68].

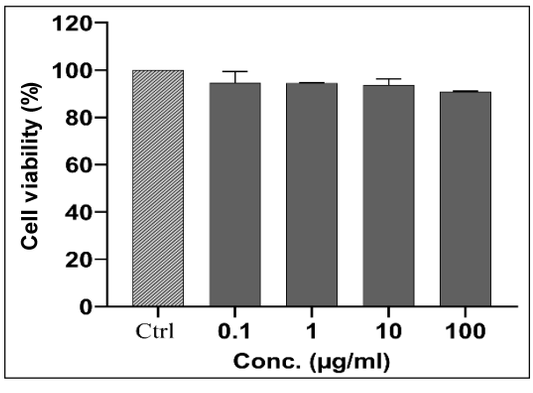

Fig. 9 Viability rates of the murine macrophage cell line (RAW 264.7) were evaluated using an SRB assay after 48 h of exposure to various concentrations of the nanocomposite PEGylated MNPs–CUR. Data are presented as the average values with error bars indicating the SD (n = 3).

It was found that PEGylated MNPs–CUR, in the concentration range of 0.1–100 μg/ml, did not affect the viability of these cells. As a result, these concentrations were used in subsequent inflammatory assays, confirming their cellular safety.

Nitric oxide inhibition assay

Since neuroinflammation is a common feature across all NDDs originating from the CNS, it leads to compromise of the BBB. This breach allows immune cells such as macrophages, neutrophils, and leukocytes to infiltrate the lesion area through the disrupted BBB [69]. A critical consequence of this infiltration is the release of inflammation-associated mediators by macrophages, with NO being a notable inflammatory mediator. Given the significant role of NO in inflammatory signaling, as mentioned in previous reports [70, 71], the ability of PEGylated MNPs–CUR to suppress NO production in LPS-stimulated RAW 264.7 cells was explored. The LPS concentration used (1 μg/mL) was selected based on various studies that assessed inflammation in RAW 264.7 cells [72–74]. Quercetin was used as a positive control because of its well-documented potent anti-inflammatory effects [75, 76].

As shown in Fig. 10, LPS treatment significantly increased the NO levels, as determined using the Griess method. However, treatment with PEGylated MNPs–CUR resulted in a dose-dependent reduction in the production of NO. Specifically, PEGylated MNP–CUR concentrations of 0.1 and 10 μg/mL significantly lowered the NO level ($P < 0.01$), while the 100 μg/mL concentration led to a 40% inhibition of NO ($P < 0.001$). This reduction matched the efficacy of quercetin at 300 μg/mL, suggesting that PEGylated MNPs–CUR are three times more potent than quercetin in inhibiting NO.

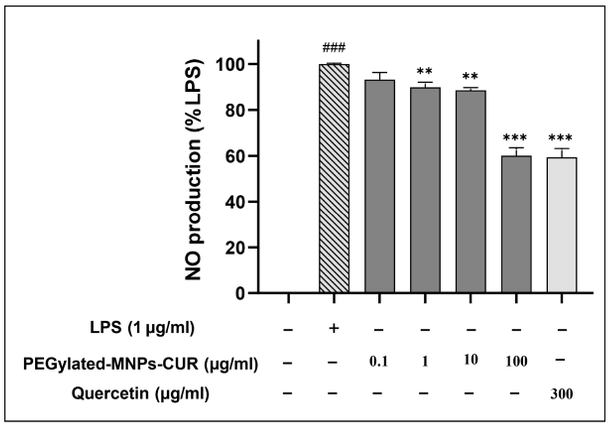

Fig. 10 Impact of PEGylated MNPs–CUR on nitric oxide (NO) production following LPS induction. Quercetin (300 μg/mL) served as a positive control for NO quantification. The data are presented as mean ± SD from three separate experiments. (*$P < 0.05$, **$P < 0.01$, and ***$P < 0.001$ compared with LPS-treated cells.)

SH-SY5Y cell line

The SH-SY5Y cell line is a useful tool for exploring the cellular processes related to disorders of the nervous system. It is also vital for efficiently screening potential therapeutics for neurological disorders [77, 78]. This cell line has also been employed to study the functions of the BBB as it effectively mimics the structure and function of a normal BBB. This makes these cells a valuable tool in

research focused on understanding the BBB characteristics in NDDs [79]. Hence, the SH-SY5Y cell line was used here to examine the impact of various compounds on cell viability. The MTT assay was employed to assess the cytotoxicity of various concentrations of MNPs, PEGylated MNPs, and PEGylated MNPs–CUR (1.56–100 μg/mL) on SH-SY5Y cells. This drug concentration range was selected based on previous studies using SH-SY5Y cells to ensure consistency with the current research [80–82].

The results in Fig. 11 demonstrate that all nanoformulations maintained high cell viability across concentrations, even at the highest one (100 μg/mL). Specifically, MNPs at the highest tested concentration resulted in a moderate reduction in cell viability to 70.5%, corresponding to 29.5% cell death. Conversely, PEGylated MNPs and PEGylated MNPs–CUR exhibited improved safety profiles at higher concentrations, with cell viability rates of 73.5% and 73%, respectively. These findings suggest that all of the tested formulations are biocompatible with neural cells. This aligns with the findings of Hibono's recent study, which established that the cell toxicity criteria required cell viability to be at least 60% compared with the control group [83]. In addition, coupled with the anti-inflammatory effects observed in earlier assays, these results support the potential of these nanoformulations as neuroprotective agents against NDDs.

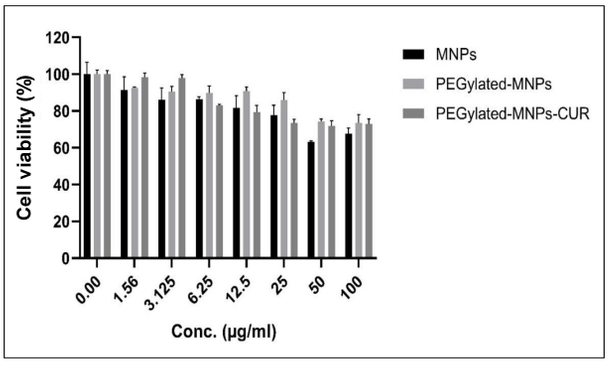

Fig. 11 Cytotoxicity on SH-SY5Y cells after 48 h of exposure to various concentrations of green synthesized MNPs, PEGylated MNPs, and PEGylated MNPs–CUR, demonstrating differential cellular responses to each treatment. Data are presented as the average values with error bars indicating the standard deviation (n = 3).

Conclusion and Future Directions

In conclusion, our study demonstrated that PEGylated MNPs, synthesized using plant polyphenols from CBS extract and loaded with CUR, exhibit significant promise as potential neuroprotective agents against NDDs. The resulting nanoparticles were spherical in shape and exhibited superparamagnetic behavior, along with efficient drug loading and controlled-release properties following the Higuchi kinetic model. Moreover, *in vitro* assessments in SH-SY5Y cells confirmed that these cells maintained high viability in the presence of the MNPs, indicating the biosafety of the nanoformulations. Furthermore, in LPS-induced RAW 264.7 cells, the PEGylated MNPs–CUR were associated with high cell viability and effectively reduced NO production, proving their anti-inflammatory potential. These findings highlight the benefits of synthesized nanoparticles in exerting anti-inflammatory effects, which are crucial in mitigating the progression of NDDs. Therefore, PEGylated MNPs–CUR present a promising therapeutic option for brain-related diseases, warranting further *in vivo* studies and clinical evaluations to fully establish their efficacy and safety. To advance PEGylated MNPs–CUR as a therapeutic for brain-related diseases, future work should focus on assessing cell inflammation-related gene expression to elucidate the underlying molecular mechanisms. It is also essential to explore delivery methods and conduct preliminary *in vivo* biocompatibility studies. Finally, it is crucial to investigate the impact of different polymer thicknesses on drug release and loading profiles, in order to optimize this approach for clinical applications.

CRediT Author Statement

Mohamed Abdelmonem: conceptualization, methodology, investigation, original draft preparation, and software. **Mohamed Ahmed Ibrahim:** methodology, original draft preparation, and visualization. **Maha A. Alhaddad:** software, visualization, and investigation. **Norazalina Bint Saad:** supervision, investigation, and methodology. **Huey Fang Teh:** supervision, methodology, writing-reviewing and editing. **Ahmad Kamil Jafaar:** supervision, writing- reviewing and editing. **Che Azurahanim Che Abdullah:** writing-reviewing and editing, supervision, and validation.

Acknowledgements

The authors extend their gratitude to the Deputy Director-General of the Malaysian Cocoa Board (MCB) and the Director of Upstream Technology Cocoa for granting permission to publish this paper and for their review. We also appreciate their provision of plant materials for our research.

Conflict of Interests

The authors reported no conflict of interest.

References

[1] M. Tsakiri, I. Tsichlis, C. Zivko, et al. Lipidic nanoparticles, extracellular vesicles and hybrid platforms as advanced medicinal products: Future therapeutic prospects for neurodegenerative diseases. *Pharmaceutics*, 2024, 16(3): 350. https://doi.org/10.3390/pharmaceutics16030350

[2] C. Mathieu, R.V. Pappu, J.P. Taylor. Beyond aggregation: Pathological phase transitions in neurodegenerative disease. *Science*, 2020, 370(6512): 56−60. https://doi.org/10.1126/science.abb8032

[3] S. Tiwari, V. Atluri, A. Kaushik, et al. Alzheimer's disease: Pathogenesis, diagnostics, and therapeutics. *International Journal of Nanomedicine*, 2019, 14: 5541−5554. https://doi.org/10.2147/ijn.s200490

[4] T.A. Enache, A.M. Oliveira-Brett. Alzheimer's disease amyloid beta peptides *in vitro* electrochemical oxidation. *Bioelectrochemistry*, 2017, 114: 13−23. https://doi.org/10.1016/j.bioelechem.2016.11.003

[5] I. Zahoor, A. Shafi, E. Haq. Pharmacological treatment of Parkinson's disease. In: Parkinson's Disease: Pathogenesis and Clinical Aspects. Brisbane (AU): Codon Publications, 2018: 129−144. https://doi.org/10.15586/codonpublications.parkinsonsdisease.2018.ch7

[6] C. Tonda-Turo, N. Origlia, C. Mattu, et al. Current limitations in the treatment of Parkinson's and Alzheimer's diseases: State-of-the-art and future perspective of polymeric carriers. *Current Medicinal Chemistry*, 2019, 25(41): 5755−5771. https://doi.org/10.2174/0929867325666180221125759

[7] S. Hewlings, D. Kalman. Curcumin: A review of its effects on human health. *Foods*, 2017, 6(10): 92. https://doi.org/10.3390/foods6100092

[8] N. Kandezi, M. Mohammadi, M. Ghaffari, et al. Novel insight to neuroprotective potential of curcumin: A mechanistic review of possible involvement of mitochondrial biogenesis and PI3/Akt/ GSK3 or PI3/Akt/CREB/BDNF signaling pathways. *International Journal of Molecular and Cellular Medicine*, 2020, 9(1): 1−32. https://doi.org/10.22088/IJMCM.BUMS.9.1.1

[9] H.Q. Lv, Y. Wang, X.T. Yang, et al. Application of curcumin nanoformulations in Alzheimer's disease: Prevention, diagnosis and treatment. *Nutritional Neuroscience*, 2023, 26(8): 727−742. https://doi.org/10.1080/1028415x.2022.2084550

[10] J. Jeevanandam, A. Barhoum, Y.S. Chan, et al. Review on nanoparticles and nanostructured materials: History, sources, toxicity and regulations. *Beilstein Journal of Nanotechnology*, 2018, 9: 1050−1074. https://doi.org/10.3762/bjnano.9.98

[11] I. Khan, K. Saeed, I. Khan. Nanoparticles: Properties, applications and toxicities. *Arabian Journal of Chemistry*, 2019, 12(7): 908−931. https://doi.org/10.1016/j.arabjc.2017.05.011

[12] M.R. Ghazanfari, M. Kashefi, S.F. Shams, et al. Perspective of Fe_3O_4Nanoparticles role in biomedical applications. *Biochemistry Research International*, 2016, 2016: 7840161. https://doi.org/10.1155/2016/7840161

[13] A. A. Hernández-Hernández, G. Aguirre-Álvarez, R. Cariño-Cortés, et al. Iron oxide nanoparticles: synthesis, functionalization, and applications in diagnosis and treatment of cancer. *Chemical Papers*, 2020, 74(11): 3809−3824. https://doi.org/10.1007/s11696-020-01229-8

[14] Y.X. Liu, W.J. Zhu, D. Wu, et al. Electrochemical determination of dopamine in the presence of uric acid using palladium-loaded mesoporous Fe_3O_4 nanoparticles. *Measurement*, 2015, 60: 1−5. https://doi.org/10.1016/j.measurement.2014.09.067

[15] N. Sher, M. Ahmed, N. Mushtaq, et al. Acetylcholinesterase activity in the brain of rats: Presence of an inhibitor of enzymatic activity in *Heliotropium eichwaldi* L. induced silver/gold allied bimetallic nanoparticles. *Nano Biomedicine and Engineering*, 2023, 15(3): 317−329. https://doi.org/10.26599/nbe.2023.9290034

[16] Z. Ait Bachir, Y.K. Huang, M.Y. He, et al. Effects of PEG surface density and chain length on the pharmacokinetics and biodistribution of methotrexate-loaded chitosan nanoparticles. *International Journal of Nanomedicine*, 2018, 13: 5657−5671. https://doi.org/10.2147/ijn.s167443

[17] J.S. Suk, Q.G. Xu, N. Kim, et al. PEGylation as a strategy for improving nanoparticle-based drug and gene delivery. *Advanced Drug Delivery Reviews*, 2016, 99: 28−51. https://doi.org/10.1016/j.addr.2015.09.012

[18] G. Gahlawat, A.R. Choudhury. A review on the biosynthesis of metal and metal salt nanoparticles by microbes. *RSC Advances*, 2019, 9(23): 12944−12967. https://doi.org/10.1039/C8RA10483B

[19] M.A. Martín, S. Ramos. Cocoa polyphenols in oxidative stress: Potential health implications. *Journal of Functional Foods*, 2016, 27: 570−588. https://doi.org/10.1016/j.jff.2016.10.008

[20] M. Martín, S. Ramos, I. Cordero-Herrero, et al. Cocoa phenolic extract protects pancreatic beta cells against oxidative stress. *Nutrients*, 2013, 5(8): 2955−2968. https://doi.org/10.3390/nu5082955

[21] M. Akrami, M. Khoobi, M. Khalilvand-Sedagheh, et al. Evaluation of multilayer coated magnetic nanoparticles as biocompatible curcumin delivery platforms for breast cancer treatment. *RSC Adv*, 2015, 5: 88096−88107. https://doi.org/10.1039/C5RA13838H

[22] I.A. Walbi, M.Z. Ahmad, J. Ahmad, et al. Development of a curcumin-loaded lecithin/chitosan nanoparticle utilizing a Box-Behnken design of experiment: Formulation design and influence of process parameters. *Polymers*, 2022, 14(18): 3758. https://doi.org/10.3390/polym14183758

[23] Y.J. Lv, J.J. Li, H.L. Chen, et al. Glycyrrhetinic acid-functionalized mesoporous silica nanoparticles as hepatocellular carcinoma-targeted drug carrier. *International Journal of Nanomedicine*, 2017, 12: 4361−4370. https://doi.org/10.2147/ijn.s135626

[24] A. van Tonder, A.M. Joubert, A.D. Cromarty. Limitations of the 3-(4, 5-dimethylthiazol-2-yl)-2, 5-diphenyl-2H-tetrazolium bromide (MTT) assay when compared to

three commonly used cell enumeration assays. *BMC Research Notes*, 2015, 8(1): 47. https://doi.org/10.1186/s13104-015-1000-8

[25] W.M. Xue, Y.Y. Liu, N. Zhang, et al. Effects of core size and PEG coating layer of iron oxide nanoparticles on the distribution and metabolism in mice. *International Journal of Nanomedicine*, 2018, 13: 5719−5731. https://doi.org/10.2147/ijn.s165451

[26] M.F. Tai, C.W. Lai, S.B. Abdul Hamid. Facile synthesis polyethylene glycol coated magnetite nanoparticles for high colloidal stability. *Journal of Nanomaterials*, 2016, 2016: 8612505. https://doi.org/10.1155/2016/8612505

[27] R. Panday, A.M.E. Abdalla, M. Yu, et al. Functionally modified magnetic nanoparticles for effective siRNA delivery to prostate cancer cells *in vitro*. *Journal of Biomaterials Applications*, 2020, 34(7): 952–964. https://doi.org/10.1177/0885328219886953

[28] S. Arsalani, Y. Hadadian, E.E. Mazon, et al. Uniform size PEGylated iron oxide nanoparticles as a potential theranostic agent synthesized by a simple optimized coprecipitation route. *Journal of Magnetism and Magnetic Materials*, 2022, 564: 170091. https://doi.org/10.1016/j.jmmm.2022.170091

[29] M. Szekeres, I. Tóth, E. Illés, et al. Chemical and colloidal stability of carboxylated core-shell magnetite nanoparticles designed for biomedical applications. *International Journal of Molecular Sciences*, 2013, 14(7): 14550−14574. https://doi.org/10.3390/ijms140714550

[30] E. Joseph, G. Singhvi. Multifunctional nanocrystals for cancer therapy: a potential nanocarrier. In: Nanomaterials for Drug Delivery and Therapy. Amsterdam: Elsevier, 2019: 91–116. https://doi.org/10.1016/b978-0-12-816505-8.00007-2

[31] M. Afrouz, F. Ahmadi-Nouraldinvand, S.G. Elias, et al. Green synthesis of spermine coated iron nanoparticles and its effect on biochemical properties of Rosmarinus officinalis. *Scientific Reports*, 2023, 13(1): 775. https://doi.org/10.1038/s41598-023-27844-5

[32] N.D. Kandpal, N. Sah, R. Loshali, et al. Co-precipitation method of synthesis and characterization of iron oxide nanoparticles. *Journal of Scientific & Industrial Research*, 2014, 73(2): 87−90.

[33] H.L. Ma, X.R. Qi, Y. Maitani, et al. Preparation and characterization of superparamagnetic iron oxide nanoparticles stabilized by alginate. *International Journal of Pharmaceutics*, 2007, 333(1-2): 177−186. https://doi.org/10.1016/j.ijpharm.2006.10.006

[34] R.A. Nyquist, R. O. Kagel. Handbook of Infrared and Raman Spectra of Inorganic Compounds and Organic Salts: Infrared Spectra of Inorganic Compounds, vol. 4. Academic press, 2012.

[35] K.O. Saygi, E. Cacan. Antioxidant and cytotoxic activities of silver nanoparticles synthesized using Tilia cordata flowers extract. *Materials Today Communications*, 2021, 27: 102316. https://doi.org/10.1016/j.mtcomm.2021.102316

[36] W.J. Chen, Y.T. Xu, D.C. Yang, et al. Preparation of liposomes coated superparamagnetic iron oxide nanoparticles for targeting and imaging brain glioma. *Nano Biomedicine and Engineering*, 2022, 14(1): 71−80. https://doi.org/10.5101/nbe.v14i1.p71-80

[37] A.B. Gorospe, S.C. Buenviaje, Y.G. Edañol, et al. One-step co-precipitation synthesis of water-stable poly(ethylene glycol)-coated magnetite nanoparticles. *Journal of Physics: Conference Series*, 2019, 1191: 012059. https://doi.org/10.1088/1742-6596/1191/1/012059

[38] B. Khatun, N. Banik, A. Hussain, et al. Genipin crosslinked curcumin loaded chitosan/montmorillonite K-10 (MMT) nanoparticles for controlled drug delivery applications. *Journal of Microencapsulation*, 2018, 35(5): 439−453. https://doi.org/10.1080/02652048.2018.1524524

[39] D. Farhanian, G. De Crescenzo, J.R. Tavares. Large-scale encapsulation of magnetic iron oxide nanoparticles via syngas photo-initiated chemical vapor deposition. *Scientific Reports*, 2018, 8: 12223. https://doi.org/10.1038/s41598-018-30802-1

[40] S.A. Kulkarni, S.S. Feng. Effects of particle size and surface modification on cellular uptake and biodistribution of polymeric nanoparticles for drug delivery. *Pharmaceutical Research*, 2013, 30(10): 2512−2522. https://doi.org/10.1007/s11095-012-0958-3

[41] L. Ribovski, N.M. Hamelmann, J.M.J. Paulusse. Polymeric nanoparticles properties and brain delivery. *Pharmaceutics*, 2021, 13(12): 2045. https://doi.org/10.3390/pharmaceutics13122045

[42] S. Ohta, E. Kikuchi, A. Ishijima, et al. Investigating the optimum size of nanoparticles for their delivery into the brain assisted by focused ultrasound-induced blood–brain barrier opening. *Scientific Reports*, 2020, 10: 18220. https://doi.org/10.1038/s41598-020-75253-9

[43] P.B. Shete, R.M. Patil, R.S. Ningthoujam, et al. Magnetic core-shell structures for magnetic fluid hyperthermia therapy application. *New Journal of Chemistry*, 2013, 37(11): 3784−3792. https://doi.org/10.1039/c3nj00862b

[44] M. Bañobre-López, A. Teijeiro, J. Rivas. Magnetic nanoparticle-based hyperthermia for cancer treatment. *Reports of Practical Oncology and Radiotherapy*, 2013, 18(6): 397−400. https://doi.org/10.1016/j.rpor.2013.09.011

[45] M. Nadeem, M. Ahmad, M.S. Akhtar, et al. Magnetic properties of polyvinyl alcohol and doxorubicine loaded iron oxide nanoparticles for anticancer drug delivery applications. *PLoS One*, 2016, 11(6): e0158084. https://doi.org/10.1371/journal.pone.0158084

[46] Z. Özcan, A.B. Hazar Yoruç. Vinorelbine-loaded multifunctional magnetic nanoparticles as anticancer drug delivery systems: Synthesis, characterization, and *in vitro* release study. *Beilstein Journal of Nanotechnology*, 2024, 15: 256−269. https://doi.org/10.3762/bjnano.15.24

[47] J. Shen, J.T. Zhang, W.T. Wu, et al. Biocompatible anisole-nonlinear PEG core–shell nanogels for high loading capacity, excellent stability, and controlled release of curcumin. *Gels*, 2023, 9(9): 762. https://doi.org/10.3390/gels9090762

[48] Z.F. Liu, M. Chiu, W. Jiang, et al. Enhancement of curcumin oral absorption and pharmacokinetics of curcuminoids and curcumin metabolites in mice. *Cancer Chemotherapy and Pharmacology*, 2012, 69(3): 679−689. https://doi.org/10.1007/s00280-011-1749-y

[49] A.V. Angarita, A. Umaña-Perez, L.D. Perez. Enhancing the performance of PEG-*b*-PCL-based nanocarriers for curcumin through its conjugation with lipophilic biomolecules. *Journal of Bioactive and Compatible Polymers*, 2020, 35(4-5): 399−413. https://doi.org/10.1177/0883911520944416

[50] L. Moradkhannejhad, M. Abdouss, N. Nikfarjam, et al. The effect of molecular weight and content of PEG on in vitro drug release of electrospun curcumin loaded PLA/PEG nanofibers. *Journal of Drug Delivery Science and Technology*, 2020, 56(Part A): 101554. https://doi.org/10.1016/j.jddst.2020.101554

[51] W. Arozal, M. Louisa, D. Rahmat, et al. Development, characterization and pharmacokinetic profile of chitosan-sodium tripolyphosphate nanoparticles based drug delivery systems for curcumin. *Advanced Pharmaceutical Bulletin*, 2020, 11(1): 77−85. https://doi.org/10.34172/apb.2021.008

[52] A. Fattahi Bafghi, B.F. Haghirosadat, F. Yazdian, et al. A

novel delivery of curcumin by the efficient nanoliposomal approach against *Leishmania major*. *Preparative Biochemistry & Biotechnology*, 2021, 51(10): 990–997. https://doi.org/10.1080/10826068.2021.1885045

[53] A.S. Joshi, H.S. Patel, V.S. Belgamwar, et al. Solid lipid nanoparticles of ondansetron HCl for intranasal delivery: development, optimization and evaluation. *Journal of Materials Science Materials in Medicine*, 2012, 23: 2163−2175. https://doi.org/10.1007/s10856-012-4702-7

[54] H.P. Le Khanh, Á. Haimhoffer, D. Nemes, et al. Effect of molecular weight on the dissolution profiles of PEG solid dispersions containing ketoprofen. *Polymers*, 2023, 15(7): 1758. https://doi.org/10.3390/polym15071758

[55] A.A. D'souza, R. Shegokar. Polyethylene glycol (PEG): A versatile polymer for pharmaceutical applications. *Expert Opinion on Drug Delivery*, 2016, 13(9): 1257−1275. https://doi.org/10.1080/17425247.2016.1182485

[56] A. Rahma, M.M. Munir, A. Khairurrijal, et al. Intermolecular interactions and the release pattern of electrospun curcumin-polyvinyl(pyrrolidone) fiber. *Biological and Pharmaceuical Bulletin*, 2016, 39(2): 163−173. https://doi.org/10.1248/bpb.b15-00391

[57] H. Rachmawati, Y.L. Yanda, A. Rahma, et al. Curcumin-loaded PLA nanoparticles: formulation and physical evaluation. *Scientia Pharmaceutica*, 2016, 84(1): 191−202. https://doi.org/10.3797/scipharm.ISP.2015.10

[58] S. Bisht, G. Feldmann, S. Soni, et al. Polymeric nanoparticle-encapsulated curcumin ("nanocurcumin"): A novel strategy for human cancer therapy. *Journal of Nanobiotechnology*, 2007, 5(1): 3. https://doi.org/10.1186/1477-3155-5-3

[59] M.L. Laracuente, M.H. Yu, K.J. McHugh. Zero-order drug delivery: State of the art and future prospects. *Journal of Controlled Release*, 2020, 327: 834−856. https://doi.org/10.1016/j.jconrel.2020.09.020

[60] D. Wojcik-Pastuszka, J. Krzak, B. Macikowski, et al. Evaluation of the release kinetics of a pharmacologically active substance from model intra-articular implants replacing the cruciate ligaments of the knee. *Materials*, 2019, 12(8): 1202. https://doi.org/10.3390/ma12081202

[61] D.R. Paul. Elaborations on the Higuchi model for drug delivery. *International Journal of Pharmceutics*, 2011, 418(1): 13−17. https://doi.org/10.1016/j.ijpharm.2010.10.037

[62] P. Trucillo. Drug carriers: A review on the most used mathematical models for drug release. *Processes*, 2022, 10(6): 1094. https://doi.org/10.3390/pr10061094

[63] O. Sreekanth Reddy, M.C.S. Subha, T. Jithendra, et al. Curcumin encapsulated dual cross linked sodium alginate/montmorillonite polymeric composite beads for controlled drug delivery. *Journal of Pharmaceutical Analysis*, 2021, 11(2): 191−199. https://doi.org/10.1016/j.jpha.2020.07.002

[64] H.H. Gustafson, D. Holt-Casper, D.W. Grainger, et al. Nanoparticle uptake: The phagocyte problem. *Nano Today*, 2015, 10(4): 487−510. https://doi.org/10.1016/j.nantod.2015.06.006

[65] M.A. Solaiman, M.A. Ali, N.M. Abdel-Moein, et al. Synthesis of Ag-NPs developed by green-chemically method and evaluation of antioxidant activities and anti-inflammatory of synthesized nanoparticles against LPS-induced NO in RAW 264.7 macrophages. *Biocatalysis and Agricultural Biotechnology*, 2020, 29: 101832. https://doi.org/10.1016/j.bcab.2020.101832

[66] E.H. Lee, Y.J. Cho. Responses of inflammation signaling pathway by saucerneol D from elicitor-treated *Saururus chinensis* on pro-inflammatory responses in LPS-stimulated Raw 264.7 cell. *Applied Biological Chemistry*, 2021, 64(1): 24. https://doi.org/10.1186/s13765-020-00585-z

[67] Z.M. Liu, W.Q. Li, F. Wang, et al. Enhancement of lipopolysaccharide-induced nitric oxide and interleukin-6 production by PEGylated gold nanoparticles in $RAW_{264.7}$ cells. *Nanoscale*, 2012, 4(22): 7135−7142. https://doi.org/10.1039/C2NR31355C

[68] P. Singh, H. Singh, S. Ahn, et al. Pharmacological importance, characterization and applications of gold and silver nanoparticles synthesized by *Panax ginseng* fresh leaves. *Artificial Cells, Nanomedicine, and Biotechnology*, 2017, 45(7): 1415−1424. https://doi.org/10.1080/21691401.2016.1243547

[69] A. Adamu, S. Li, F.K. Gao, et al. The role of neuroinflammation in neurodegenerative diseases: Current understanding and future therapeutic targets. *Frontiers in Aging Neuroscience*, 2024, 16: 1347987. https://doi.org/10.3389/fnagi.2024.1347987

[70] I. Plastira, E. Bernhart, M. Goeritzer, et al. 1-Oleyl-lysophosphatidic acid (LPA) promotes polarization of BV-2 and primary murine microglia towards an M1-like phenotype. *Journal of Neuroinflammation*, 2016, 13(1): 205. https://doi.org/10.1186/s12974-016-0701-9

[71] R. Orihuela, C.A. McPherson, G.J. Harry. Microglial M1/M2 polarization and metabolic states. *British Journal of Pharmacology*, 2016, 173(4): 649−665. https://doi.org/10.1111/bph.13139

[72] A.M. Alnuqaydan, A.G. Almutary, M. Azam, et al. Phytantriol-based berberine-loaded liquid crystalline nanoparticles attenuate inflammation and oxidative stress in lipopolysaccharide-induced $RAW_{264.7}$ macrophages. *Nanomaterials*, 2022, 12(23): 4312. https://doi.org/10.3390/nano12234312

[73] E. Jones, I.M. Adcock, B.Y. Ahmed, et al. Modulation of LPS stimulated NF-kappaB mediated nitric Oxide Production by PKCε and JAK2 in RAW macrophages. *Journal of Inflammation*, 2007, 4(1): 23. https://doi.org/10.1186/1476-9255-4-23

[74] M.H. Rosli, N.F.M. Khairuddin, M. Abdelmonem, et al. Copper oxide nanoparticles in oil and gas industries: Current developments. In: Recent Advancements in Multidimensional Applications of Nanotechnology: Volume 1. BENTHAM SCIENCE PUBLISHERS, 2024: 49−74. https://doi.org/10.2174/9789815238846124010005

[75] Y.J. Kim, W. Park. Anti-inflammatory effect of quercetin on RAW 264.7 mouse macrophages induced with polyinosinic-polycytidylic acid. *Molecules*, 2016, 21(4): 450. https://doi.org/10.3390/molecules21040450

[76] T. Li, F. Li, X.Y. Liu, et al. Synergistic anti-inflammatory effects of quercetin and catechin *via* inhibiting activation of TLR4–MyD88-mediated NF-κB and MAPK signaling pathways. *Phytotherapy Research*, 2019, 33(3): 756−767. https://doi.org/10.1002/ptr.6268

[77] Y. Peng, S. Chu, Y. Yang, et al. Neuroinflammatory *in vitro* cell culture models and the potential applications for neurological disorders. *Frontiers in Pharmacology*, 2021, 12: 671734. https://doi.org/10.3389/fphar.2021.671734

[78] L. Strother, G.B. Miles, A.R. Holiday, et al. Long-term culture of SH-SY5Y neuroblastoma cells in the absence of neurotrophins: A novel model of neuronal ageing. *Journal of Neuroscience Methods*, 2021, 362: 109301. https://doi.org/10.1016/j.jneumeth.2021.109301

[79] T. Toimela, H. Mäenpää, M. Mannerström, et al. Development of an *in vitro* blood–brain barrier model—Cytotoxicity of mercury and aluminum. *Toxicology and Applied Pharmacology*, 2004, 195(1): 73−82. https://doi.org/10.1016/j.taap.2003.11.002

[80] M.E. Piersimoni, X. Teng, A.E.G. Cass, et al. Antioxidant lipoic acid ligand-shell gold nanoconjugates against oxidative stress caused by α-synuclein aggregates.

Nanoscale Advances, 2020, 2(12): 5666−5681. https://doi.org/10.1039/D0NA00688B

[81] N. Ismail, M. Ismail, M.U. Imam, et al. Mechanistic basis for protection of differentiated SH-SY5Y cells by oryzanol-rich fraction against hydrogen peroxide-induced neurotoxicity. *BMC Complementary and Alternative Medicine*, 2014, 14(1): 467. https://doi.org/10.1186/1472-6882-14-467

[82] J. Zargan, M. Sajad, S. Umar, et al. Scorpion (*Odontobuthus doriae*) venom induces apoptosis and inhibits DNA synthesis in human neuroblastoma cells. *Molecular and Cellular Biochemistry*, 2011, 348(1-2): 173−181. https://doi.org/10.1007/s11010-010-0652-x

[83] P.R. Hibono/ Cytotoxicity test of bovine demineralized bone matrix on human mesenchymal stem cells using the mtt assay method. *Journal of Stem Cell Research and Tissue Engineering*, 2023, 7(2): 62–67. https://doi.org/10.20473/jscrte.v7i2.52559